Sandwiched SiO$_2$@Ni@ZrO$_2$ as a coke resistant nanocatalyst for dry reforming of methane

Jian Dou[a,1], Riguang Zhang[b,1], Xiaobin Hao[b], Zhenghong Bao[a], Tianpin Wu[c], Baojun Wang[b,*], Fei Yu[a,*]

[a] Department of Agricultural and Biological Engineering, Mississippi State University, MS 39762, United States
[b] Key Laboratory of Coal Science and Technology of Ministry of Education and Shanxi Province, Taiyuan University of Technology, Taiyuan, Shanxi 030024, PR China
[c] X-ray Science Division, Advanced Photon Source, Argonne National Laboratory, Argonne, IL 60439, United States

ABSTRACT

Design active and coke resistant Ni based catalysts is critical for implementation of dry reforming of methane technology. In this work, coke resistant SiO$_2$@Ni@ZrO$_2$ catalyst has been successfully prepared through precipitation of nickel nitrate with ammonia onto silica spheres, followed by coating with porous ZrO$_2$ shell. Through thermal treatment in air and hydrogen, nickel nanoparticles with size of 6 nm were sandwiched between silica core and zirconia shell. The ZrO$_2$ coated Ni catalyst exhibited a high activity of ~13.0 mol CH$_4$ per gram of Ni per hour for methane dry reforming at 700 °C, which is more than 6 times higher than that of SiO$_2$@ Ni catalyst under the same reaction condition. The SiO$_2$@Ni@ZrO$_2$ catalyst is also coke resistant as no carbon formation was observed for methane dry reforming at 700 °C for 20 h. As a comparison, carbon nanotubes formed over SiO$_2$@Ni catalyst during dry reforming reaction with a coking rate of 0.019 g of carbon formed per gram of catalyst per hour. Operando XANES/EXAFS study of SiO$_2$@Ni@ZrO$_2$ catalyst confirmed metallic Ni phase during methane dry reforming from 400 to 800 °C. Theoretical calculations suggests that ZrO$_2$ stabilized Ni clusters lowers the highest dissociation energy barrier of CH$_4$ and CO$_2$ by 1.37 and 2.56 eV comparing to bulk Ni, increasing dry reforming activity on SiO$_2$@Ni@ZrO$_2$ catalyst. Furthermore, the higher binding energy of CO$_2$ over CH$_4$ on SiO$_2$@Ni@ZrO$_2$ leads to enrichment of CO$_2$ on catalyst surface, which mitigates coke formation.

1. Introduction

Dry reforming of methane (DRM) with carbon dioxide is a promising reaction to utilize methane from surplus natural gas supply to produce syngas, which is the important chemical intermediate for Fischer-Tropsch synthesis and methanol synthesis [1,2]. The syngas produced from DRM reaction with a relatively low H$_2$/CO ratio is an ideal feedstock to be blended with stream from steam reforming of methane to adjust the ratio of H$_2$/CO mixture for Fischer–Tropsch synthesis and methanol synthesis [3–7]. Furthermore, DRM reaction converts the greenhouse gas, CO$_2$ to valuable chemicals and mitigates emission of CO$_2$ to environment [8–10].

Nickel based catalysts have been widely used for DRM reaction due to their catalytic activities comparable to noble metal catalysts [11–15]. However, many of these Ni based catalysts undergo severe deactivation because of coke deposition via methane decomposition (CH$_4$ → C(s) + 2H$_2$) and CO disproportionation (Boudouard reaction: 2CO →

C(s) + CO$_2$) [16,17]. Sintering of nickel nanoparticles at high temperature during dry reforming of methane reaction is another challenge factor [18]. Other than reducing the exposed surface area of Ni, it further aggravates coke deposition when the size of Ni nanoparticles becomes larger.

Extensive efforts have been devoted to develop stable and coke resistant Ni catalysts for DRM reaction [19–27]. For example, molecular layer deposition (MLD) method has been applied to coat supported Ni nanoparticles with porous alumina film [3]. The coated porous alumina shell significantly enhanced the stability of Ni nanoparticles. Coating of nickel nanoparticles with porous shell has also been achieved using wet chemistry synthesis method [28–32]. Generally Nickel nanocrystals were prepared first, followed by coating with porous silica shell. The resulted core-shell nanocatalysts exhibit excellent performance for dry reforming reaction [8]. However, it is known that the structural stability of porous silica materials is a concern at high temperature in the presence of steam [33,34]. As water is the byproduct of reforming

---

reaction due to reverse water gas shift reaction, the long term stability of porous silica shell needs to be addressed.

In this work, nickel doped silica spheres (SiO₂@Ni) was prepared via so-gel synthesis of in ethanol solution (Fig. S1). The synthesized SiO₂@Ni spheres were then used as the core material for coating with porous zirconia shell. Finally, the formed SiO₂@Ni@ZrO₂ sample was thermally treated to decompose the organic template. The structure, morphology, and reducibility of the as-synthesized catalysts were characterized by XRD, TEM/EDX, and TPR. The prepared SiO₂@Ni and SiO₂@Ni@ZrO₂ catalysts have been investigated for methane dry reforming reaction at 200–900 °C, and the catalytic activity was measured based on methane conversion. The activation energies of CH_4 and CO_2 were determined for SiO₂@Ni and SiO₂@Ni@ZrO₂ catalysts from kinetic study. Coke resistance of the Ni catalysts with or without ZrO_2 coating was studied by examining the spent catalysts. Furthermore, computational studies were performed to understand the mechanism of methane dry reforming on Ni catalysts.

2. Experimental section

2.1. Synthesis of SiO₂@Ni spheres

In a typical synthesis, 1 mL of tetraethyl orthosilicate (TEOS, Acros, 98%) was added to 20 mL of ethanol (Fisher Chemical, HPLC grade), followed by adding 2 mL of ammonia solution (NH₄OH, Sigma-Aldrich, 28.0–30.0%). The resulted mixture was stirred at room temperature for 1 h. After that, 2.3 mL of 0.2 M nickel nitrate (Ni(NO₃)₂·6H₂O, Fisher Chemical, Certified grade) solution was added to above mixture, and was stirred at room temperature for 10 min. The product was collected by centrifugation, and was washed with ethanol for 3 times.

2.2. Preparation of SiO₂@Ni@ZrO₂ core-shell nanocatalysts

The product collected above was re-dispersed in 20 mL of ethanol, followed by adding 0.1 mL of water and 0.1 mL of briji 30 (C₂₀H₄₂O₅, Acros). The resulted mixture was stirred for 30 min, followed by adding 0.2 mL of zirconium n-butoxide (C₁₆H₃₆O₄Zr, Alfa Aesar, 80% w/w in 1-butanol). The resulted mixture was further stirred at room temperature for 16 h. The product was centrifuge and re-disperse in 20 mL of water for 1 day. The product was collected by centrifuge and washed with water for 3 times, followed by drying at 70 °C overnight. After that, the as-synthesized SiO₂@Ni and SiO₂@Ni@ZrO₂ were calcined in static air at 550 °C for 3 h, and were named as calcined SiO₂@Ni and calcined SiO₂@Ni@ZrO₂, respectively. The calcined samples were further reduced in 10%H₂/N₂ at 700 °C for 1 h, and were named as reduced SiO₂@Ni and reduced SiO₂@Ni@ZrO₂ accordingly (or simply as SiO₂@Ni and SiO₂@Ni@ZrO₂).

2.3. Characterization

The crystallographic structure of prepared SiO₂@Ni and SiO₂@Ni@ZrO₂ catalysts were studied by powder X-ray diffraction (XRD, Rigaku Ultima III, Cu K$_\alpha$ radiation, λ = 1.54059 Å) at a scanning rate of 2°/min. The morphology and chemical composition of the nanocatalysts were characterized with transmission electron microscopy coupled with energy dispersive X-ray spectroscopy (TEM/EDX, JEOL JEM-2100). The specific surface area of the core-shell catalysts was determined using N₂ adsorption and desorption analysis (Quantachrome Autosorb-1). The reducibility of nickel catalysts were examined with H₂ temperature programmed reduction (H₂-TPR, Quantachrome ChemBET Pulsar TPR/TPD). The content of Ni was determined by EDX mapping using scanning electron microscopy coupled with energy dispersive X-ray spectroscopy (SEM/EDX, Zeiss, EVO 50), with average of five measurements for each sample. The coke deposition on catalyst after dry reforming reaction was analyzed with thermogravimetric method (TGA, Shimadzu, TGA-50).

2.4. Operando X-ray absorption spectroscopy (XAS)

Operando XAS measurement of Ni K edge of nickel catalyst under reduction and reaction conditions was carried out on the bending magnet beamline 9-BM-C at the Advanced Photon Source (APS) within Argonne National Laboratory. The data was collected in transmission step-scan mode. Photon energies were selected with a double crystal Si (111) monochromator, and harmonic rejection was achieved using a rhodium coated flat mirror. The ionization chambers were optimized for 10% absorption in the incident ion chamber and 70% absorption in the X-ray detector. Ni foil standard was placed downstream of the sample cell as a reference to calibrate the photon energy of each measured spectrum. The catalyst sample was pressed as a self-supporting wafer into a cylindrical sample holder having six holes. The sample thickness was chosen to give a total absorbance (μx) at Ni K-edge between 1 and 2, and edge steps (Δμx) around $0.3 - 0.5$. The sample holder was inserted into a quartz tube reactor, which was heated by a horizontal cylindrical furnace. Continuous measurement of Ni K-edge of the catalyst was carried out under reduction and reaction conditions. The catalyst was heated from room temperature to 700 °C at 5 °C/min in the presence of 100 mL/min of 3.5%H₂/He gas flow. After reduction, the reactor was cooled to 400 °C in 100 mL/min of N₂ flow. Then, the gas was switched to 5%CH₄/5%CO₂/90%N₂, and the reactor was heated from 400 to 800 °C step wisely with the interval of 100 °C. At every reaction temperature (i.e., 400, 500, 600, 700, and 800 °C), the DRM reaction was allowed to proceed for 1 h with continuous measuring Ni K-edge. The measured XANES/EXAFS spectra was processed and fitted with IFEFFIT using Athena and Artemis programs [35,36]. The edge energy was determined from the first inflection point on the rising edge of the XANES spectra. Background subtraction was carried out using Autobk and Spline smoothing functions in the Athena program. The k-range and R-range used for the fittings are 3–13 Å^{-1} and 1–5.4 Å, respectively.

2.5. Dry reforming of methane with carbon dioxide

The methane dry reforming reaction was carried out at atmospheric pressure using a tubular quartz fixed bed reactor with inner diameter of 6 mm. In a typical experiment, 50 mg of catalysts with size of 40–60 mesh was packed into the center of the reactor using quartz wool. The thermocouple was inserted into the reactor and closed to the catalyst bed. Before reaction, the catalyst was reduced at 700 °C for 1 h in 10% H₂/N₂ gas mixture with a flow rate of 100 mL/min. After reduction, the inlet gas was switched to reactant gas mixture of CO₂/CH₄/N₂ (1:1:1) with a flow rate of 60 mL/min. For measuring activities at 200–900 °C, 20 mg of catalyst was used and the weight hourly space velocity (WHSV) was 180,000 ml g^{-1} h^{-1}. The reaction was monitored with an online gas chromatograph (GC, Agilent 7890A) coupled with flame ionized detector (FID) and thermal conductive detector (TCD). The product gas mixture was separated using Hayesep Q and MolSieve 5A columns.

3. Computational details

3.1. Calculation methods

Density functional theory (DFT) calculations are performed by projector augmented wave (PAW) method in the Vienna Ab Initio Simulation Package (VASP) [37,38]. The spin-polarized Perdew-Burke-Ernzerhof (PBE) generalized gradient approximation (GGA) functional was employed for the exchange–correlation energy [39–41]. A cutoff energy is set to 400 eV. The geometry is optimized when the forces on atoms are less than 0.03 eV/Å. The Brillouin zone is sampled by a k-point of 3 × 3 × 1 and Methfessel-Paxton smearing width is employed with 0.20 eV. The Ni bulk lattice constant and magnetic moment are calculated to be 3.524 Å and 1.63 μB per atom, which accord well with
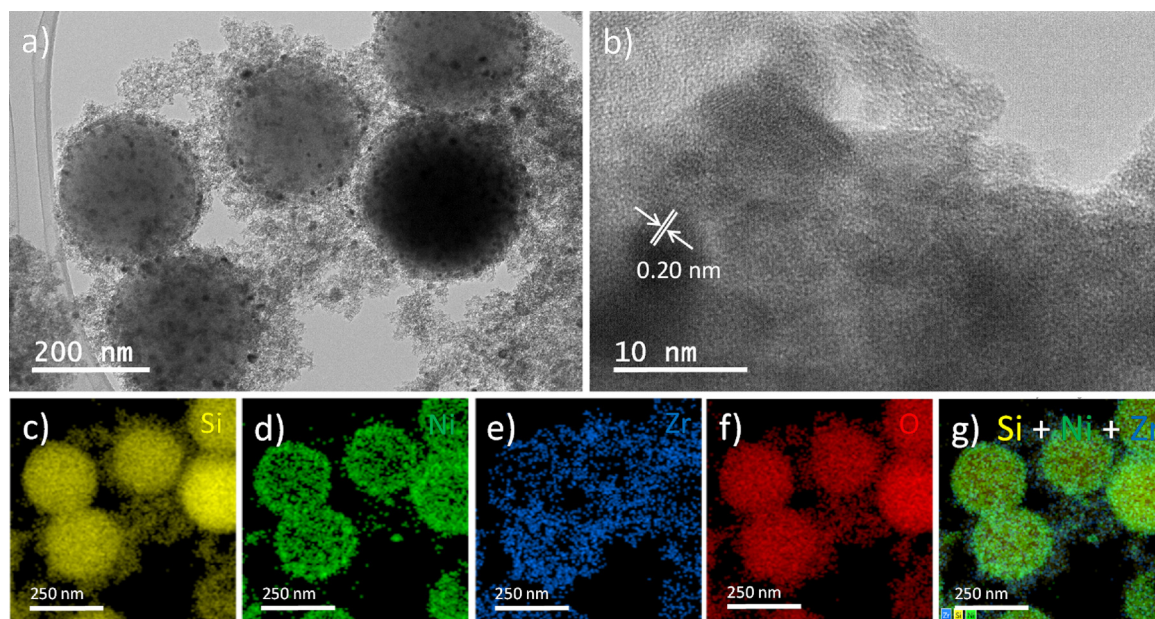
Fig. 1. (a, b) TEM images and (c–g) EDX mapping of reduced SiO$_2$@Ni@ZrO$_2$ catalysts.

the experimental values of 3.523 Å and 1.61 µB, respectively [42,43]. The Climbing-Image Nudged Elastic Band method (CI-NEB) is used to obtain the minimum energy path [44,45], which is inserted with at least four images between the initial and final states. The forces for all atoms in the transition state structures are less than 0.05 eV/Å. Moreover, the van der Waals interaction was considered for the adsorption of CH$_4$ and CO$_2$ using the DFT-D2 method of Grimme [46]. In addition, the isolated atoms and gaseous molecules are optimized in a $10 \times 10 \times 10$ Å cubic cell.

3.2. Calculation model

To simulate the large Ni nanoparticles in SiO$_2$@Ni catalyst, the close-packed Ni(111) surface with the dominantly exposed facet of face-centered cubic (FCC) metals is selected as the catalyst model. As shown in Fig. S7(a), the $p(3 \times 3)$ unit cell is cleaved with the slab thickness of four-layers, in which the top three layers and absorbed species are allowed to relax, while the bottom layers are fixed in their bulk position. The vacuum thickness of 15 Å between the repeated slabs can be maintained to exclude the slab interactions. Four adsorption sites exist: top, bridge, hcp and fcc sites (hcp and fcc are the 3-fold hollow site).

On the other hand, for the model construction of the small Ni nanoparticle in SiO$_2$@Ni@ZrO$_2$ catalyst based on the following reasons, firstly, TEM results show metallic Ni in SiO$_2$@Ni@ZrO$_2$ catalyst largely exposed the (111) plane (see the 1st paragraph in Section 4.1); secondly, in situ EXAFS also confirmed the metallic state of Ni nanoparticles under reaction condition; thirdly, the Fourier transformed EXAFS spectra confirm the Ni-Ni distance of 2.47 Å and the coordination number of 8.8 (see the 1st paragraph of Section 4.3); further, Ni nanoparticles with a size of ˜6 nm were built containing thousands of atoms, because of the large number of atoms, it is impossible for us to perform DFT calculations study on them. Thus, in this study, compared to the large Ni nanoparticle in SiO$_2$@Ni catalyst simulated by the periodic Ni(111) surface, the Ni$_{15}$ cluster is built to qualitatively reflect the largely exposed (111) plane consisted of the 3-fold hollow site, which is also the dominant surface characteristic of the small Ni nanoparticle in SiO$_2$@Ni@ZrO$_2$ catalyst. Moreover, as mentioned in this study, the calculated results using the Ni$_{15}$ cluster can well describe the catalytic performance of the small Ni nanoparticle in SiO$_2$@Ni@ZrO$_2$ catalyst. Therefore, based on the experimental characterizations by TEM and EXAFS, a Ni$_{15}$ cluster is constructed to reflect the characteristic of the

small Ni nanoparticle in SiO$_2$@Ni@ZrO$_2$ catalyst. As shown in Fig. S7(b), a Ni$_{15}$ cluster is supported on an eight-layers $p(2 \times 2)$ ZrO$_2$(111) surface, where the top four layers together with the Ni$_{15}$ cluster are relaxed, and the bottom four layers are fixed in their bulk positions. The slab is separated by 20 Å vacuum to ensure the negligible interaction between the adsorbates and the slab. There are four types of adsorption sites: top, bridge, 3-fold hollow and 4-fold hollow sites, where the Ni atom serial number was labeled to easily locate the following adsorption site in the study.

4. Results and discussion

4.1. Synthesis and characterization of SiO$_2$@Ni@ZrO$_2$ catalyst

The SiO$_2$@Ni@ZrO$_2$ core-shell nanocatalysts were prepared by a wet chemistry synthetic route. Silica spheres were synthesized by hydrolysis of TEOS in ethanol in the presence of ammonia. following a modified Stobe method [47]. After forming silica spheres, nickel nitrate solution was added to the silica synthetic solution. The opaque solution turned light blue immediately due to precipitation of nickel nitrate with ammonia on the surface of silica spheres. The resulted SiO$_2$@Ni spheres were further coated with porous ZrO$_2$ shell by hydrolysis of zirconium butoxide in water/ethanol mixture in the presence of surfactant [48]. The as-synthesized sample was further heated in air and hydrogen consecutively to burn off surfactant and reduce Ni to metallic state. The morphology of reduced SiO$_2$@Ni@ZrO$_2$ catalyst was examined by TEM. As shown in Fig. 1, the SiO$_2$@Ni@ZrO$_2$ catalyst exhibits a core-shell structure with size of around 250 nm. The surface of silica spheres is decorated with Ni nanoparticles, which has a size of ˜6 nm. The lattice spacing of 0.20 nm measured from the high resolution image can be assigned to (111) plane of cubic phase metallic Ni (JCPDS 04-0850). The Ni nanoparticles decorated silica spheres is covered with porous ZrO$_2$ shell. The core-shell structure of SiO$_2$@Ni@ZrO$_2$ is further confirmed by EDX mapping. Shown in Fig. 1c–g, Most of the Ni nanoparticles are sandwiched between silica core and zirconia shell. It shows that porous ZrO$_2$ shell is effective to stabilize 6 nm Ni nanoparticles, as the reduced SiO$_2$@Ni@ZrO$_2$ catalyst has been thermally treated at 550 °C in air and 700 °C in 10%H$_2$/N$_2$. It is noted that a few Ni nanoparticles are detached from the silica surface (Fig. 1d). By examining the region of detached Ni nanoparticles, both silica and zirconia also present in that area and encapsulate the Ni nanoparticles (Fig. 1c and
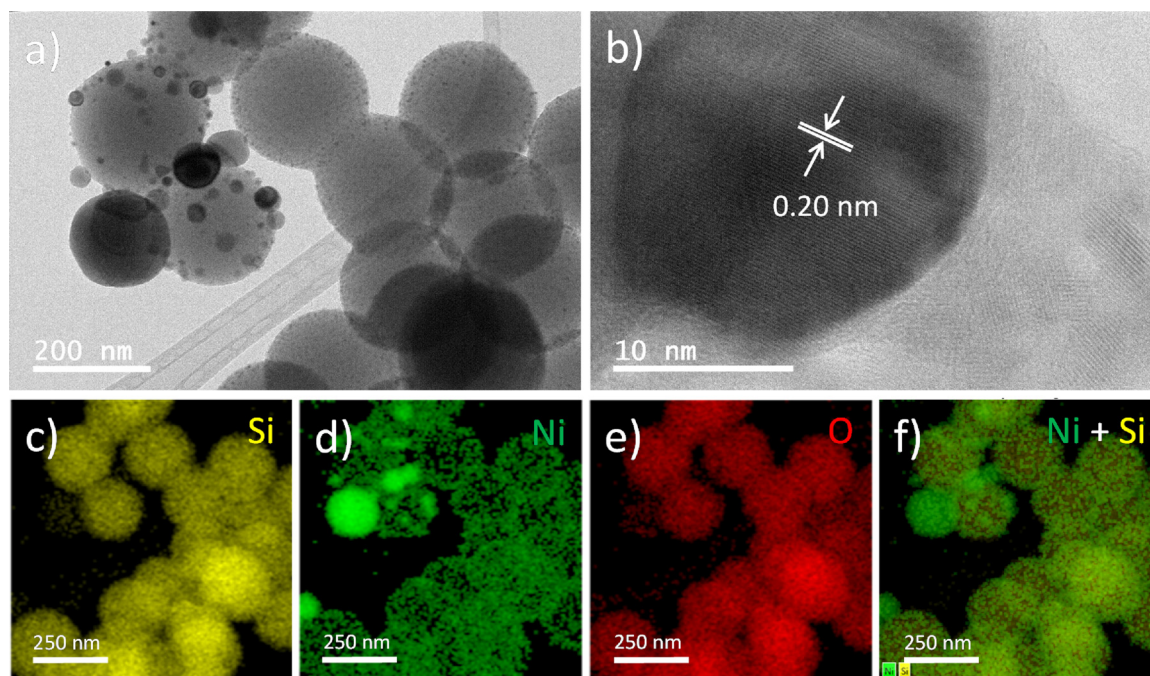
Fig. 2. (a, b) TEM images and (c–f) EDX mapping of reduced SiO₂@Ni catalysts.

e). Furthermore, from synthetic point of view, nickel was deposited onto silica surface in the presence of ammonia, which was then covered by zirconia. Without silica spheres core, precipitation of large nickel hydroxide particles is anticipated, eventually resulting in poor dispersion of Ni. As a comparison, the SiO₂@Ni catalyst without ZrO₂ coating has also been examined by TEM (Fig. 2). Unlike SiO₂@Ni@ZrO₂ sample, Ni nanoparticles in SiO₂@Ni exhibits a bimodal size distribution. In addition to 6 nm Ni nanoparticles dispersed on the surface of SiO₂ spheres, there are many large Ni particles observed with size as large as 170 nm. The presence of large Ni particle is due to sintering of Ni during thermal treatment, which further confirms the importance of ZrO₂ shell for stabilizing small Ni nanoparticles.

The crystallographic structure of SiO₂@Ni and SiO₂@Ni@ZrO₂ catalysts were examined by powder X-ray diffraction (Fig. 3a). For SiO₂@Ni, three sharp peaks appear at 44.4°, 52.0°, and 76.5°, which are attributed to (111), (200), and (220) plane of cubic metallic Ni phase (JCPDS 04-0850). The broad peak around 21.2° is due to amorphous silica spheres [49,50]. After coating with ZrO₂, only two small peaks for metallic Ni are observable at 44.4° and 52.0°. It is noted that Ni loading in SiO₂@Ni and SiO₂@Ni@ZrO₂ is 12.2 and 8.9%, respectively (Table 1). Thus the sharp decrease in the intensity of Ni peaks is most likely due to smaller Ni particles (e.g., 6 nm) in SiO₂@Ni@ZrO₂ comparing to SiO₂@Ni catalyst. The average size of Ni particles in SiO₂@Ni and SiO₂@Ni@ZrO₂ catalysts is calculated to be 33.1 and 5.6 nm from

broadening of Ni(111) peak using Scherrer equation. As the size of Ni nanoparticles in SiO₂@Ni@ZrO₂ is quite uniform, the size determined from Scherrer equation is consistent with TEM observation.

Reducibility of calcined SiO₂@Ni and calcined SiO₂@Ni@ZrO₂ samples was studied by H₂-TPR (Fig. 3b). Two reduction peaks are observed at 388 and 580 °C for calcined SiO₂@Ni sample. The first peak at 388 °C could be assigned to big NiO particles on the surface of silica spheres, which is relatively easier to be reduced [23]. The second peak at higher temperature (i.e., 580 °C) is attributed small NiO particles partially or fully covered by silica [51]. After coating with ZrO₂, there is only one reduction peak observed at 734 °C. It suggests there is strong interaction between surface NiO and ZrO₂, which stabilize Ni nanoparticles at high temperature. In the literature, a number of Ni/ZrO₂ based catalysts have been reported for methane dry reforming reaction [52–58]. It is noted that the reduction peak of Ni/ZrO₂ catalysts generally occurs at 490–550 °C [53,57]. For SiO₂@Ni@ZrO₂ catalyst, the reduction peak was observed at 734 °C, which is nearly 200 °C higher than those of Ni/ZrO₂ catalysts. It is possibly attributed to the unique core-shell structure with Ni nanoparticles assembled between silica core and zirconia shell, resulting in strong interaction between Ni and support.
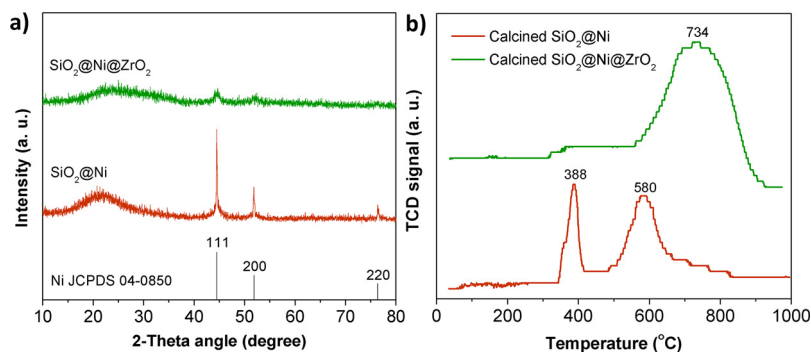

Fig. 3. (a) XRD patterns of reduced SiO₂@Ni and reduced SiO₂@Ni@ZrO₂ catalysts. (b) H₂-TPR of calcined SiO₂@Ni and calcined SiO₂@Ni@ZrO₂ samples.

Table 1
Dry reforming of methane over SiO_2@Ni@ZrO_2 catalysts.[a]

Catalyst	Ni Content (%)	Surface area (m²/ g)	Temperature (°C)	CH_4 Conversion (%)	CO_2 Conversion (%)	CO Selectivity (%)	H_2/CO ratio	Activity (mol g⁻¹ h⁻¹)[b]
SiO_2@Ni	12.2	195	500	1.3	0.4	–	–	0.28
			600	4.4	3.3	76.9	0.55	0.98
			700	9.1	7.6	88.2	0.57	1.99
			800	34.5	37.6	94.0	0.73	7.58
			900	83.4	81.5	94.7	0.95	18.31
SiO_2@Ni@ZrO_2	8.9	226	500	7.2	6.9	83.3	0.49	2.17
			600	16.3	19.0	90.3	0.54	4.90
			700	43.1	48.8	94.7	0.76	12.99
			800	79.2	80.6	95.2	0.95	23.84
			900	98.8	95.0	94.0	1.00	29.74
0.5Ni/CeNi$_x$O$_y$[c]	15.1	94	800	47.8	55.7	–	0.79	8.5
Ni$_{15}$CeMgAl[d]	15.0	243	800	99	82	–	0.80	5.9

[a] Reaction condition: CH_4:CO_2:CO = 1:1:1, 20 mg of catalyst + 0.2 g quartz sand, WHSV = 180,000 mL g⁻¹ h⁻¹, 500–800 °C, 1 bar.
[b] Activity was calculated as mole of CH_4 converted per total gram of Ni per hour.
[c] From ref. [23]. CH_4:CO_2:CO = 1:1:1, WHSV = 180,000 mL g⁻¹ h⁻¹.
[d] From ref. [9]. CH_4:CO_2 = 1.04:1, GHSV = 48,000 h⁻¹.

4.2. Methane dry reforming over Ni core-shell catalysts

The reduced SiO_2@Ni and SiO_2@Ni@ZrO_2 catalysts have been investigated for dry reforming of methane reaction at 200–900 °C (Fig. 4 and Fig. S3). For SiO_2@Ni catalyst, the reaction starts at around 500 °C with conversion of CH_4 as 1.3 and 4.4% at 500 and 600 °C, respectively. The conversion of CH_4 increases to 9.1 and 34.5% at 700 and 800 °C accordingly. At 900 °C, the CH_4 conversion reaches 83.4%. Similarly, the initial conversion of CO_2 at below 600 °C is less than 5%. Increasing the reaction temperature to 700, 800 and 900 °C, the CO_2 conversion increases to 43.1, 79.2, and 98.8% at, respectively. By coating SiO_2@Ni with ZrO_2 shell, the methane dry reforming activity improves significantly. At 500 °C, both of the conversions for CH_4 and CO_2 are higher than 5%, as 7.2 and 6.9% accordingly. The activity was calculated as mole of CH_4 formed per total gram of Ni per hour. The activity of SiO_2@Ni@ZrO_2 catalyst is 2.17 mol g⁻¹ h⁻¹ at 500 °C, which is 7 times higher than that of SiO_2@Ni catalyst (0.28 mol g⁻¹ h⁻¹). Increasing the reaction temperature to 600 and 700 °C, the CH_4 conversion increases to 16.3 and 43.1%, while the CO_2 conversion increases to 19.0 and 48.8%, respectively. The activity of SiO_2@Ni@ZrO_2 catalyst is 4.90 and 12.99 mol g⁻¹ h⁻¹ at 600 and 700 °C, which is 5–6 times higher than that of SiO_2@Ni catalyst at the same reaction temperature. At 800 °C, the activity of SiO_2@Ni@ZrO_2 catalyst is 23.84 mol g⁻¹ h⁻¹, which is about 2.8–4.0 times higher than previous reported 0.5Ni/ CeNi$_x$O$_y$ (8.5 mol g⁻¹ h⁻¹) and Ni$_{15}$CeMgAl (5.9 mol g⁻¹ h⁻¹) catalysts under similar reaction conditions. At 900 °C, more than 95% conversion of CH_4 and CO_2 conversion is achieved for SiO_2@Ni@ZrO_2 catalyst. It was observed that the H_2/CO ratio is less 1, which was attributed to the reaction between H_2 and CO_2 to generate H_2O and CO via reverse water gas shift reaction, as suggested by the equilibrium profile of dry reforming reaction (Fig. S4).

The coking resistance of SiO_2@Ni and SiO_2@Ni@ZrO_2 catalysts were studied by examining the spent catalysts after dry reforming reaction at 700 °C for 20 h with a total flowrate of 60 mL/min (CH_4:CO_2:N_2 = 1:1:1). Fig. 5a presents the XRD patterns of spent SiO_2@Ni and SiO_2@Ni@ZrO_2 catalysts. Similar as fresh catalysts, the peaks at 44.5, 51.8, and 76.5° are attributed to (111), (200), and (220) plane of metallic Ni. For spent SiO_2@Ni catalyst, there is additional peak observed at 26.4°, which is assigned to (002) plane of graphitic carbon [59,60]. It shows that carbon was formed on SiO_2@Ni catalyst during dry reforming reaction, either from decomposition of CH_4 and/ or disproportionation of CO. However, there is no carbon peak in the XRD pattern for spent SiO_2@Ni@ZrO_2 catalyst, suggesting that SiO_2@ Ni@ZrO_2 is a carbon resistant catalyst for dry reforming reaction. The coke resistance of SiO_2@Ni@ZrO_2 is attributed to porous ZrO_2 coating, which stabilize small Ni nanoparticles during thermal treatment and dry reforming reaction and inhibits carbon deposition on catalyst surface.

The amount of deposited carbon was analyzed by thermogravimetric experiment. The spent catalyst was heated in air up to 900 °C, and the weight change of catalyst was monitored continuously. Shown in Fig. 5b, there is no change of weight for spent SiO_2@Ni@ZrO_2 catalyst, further confirming that no carbon deposition on SiO_2@Ni@ZrO_2 catalyst during dry reforming reaction. On the contrary, there is weight loss observed from 500 to 730 °C for SiO_2@Ni catalyst, which is attributed to burn off of graphitic carbon [61,62]. Based on the total weight loss of 28% for SiO_2@Ni catalyst, the coking rate (defined as gram of carbon formed per gram of catalyst per hour) is calculated to be 0.019 g g⁻¹ h⁻¹. It was noted that there was small amount (i.e., ~ 0.5–1.0 wt%) of weight gain at ~300−500 °C (Fig. 5b), possibly due to oxidation of supported nanoparticles to nickel oxide.

The spent catalysts were further characterized by TEM to examine
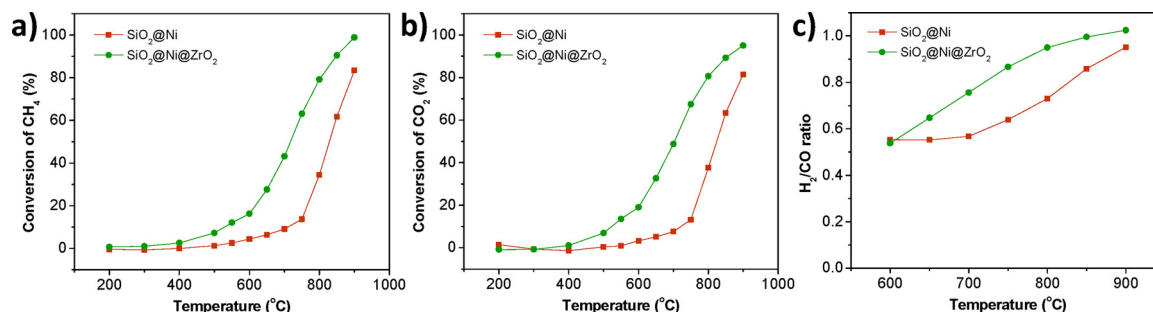
Fig. 4. Dry reforming of CH_4 with CO_2 over SiO_2@Ni and SiO_2@Ni@ZrO_2 catalysts: (a) conversion of CH_4, (b) conversion of CO_2, and (c) H_2/CO ratio. Reaction condition: 20 mg of catalyst + 0.2 g quartz sand, CH_4:CO_2:N_2 = 1:1:1, WHSV = 180,000 mL g⁻¹ h⁻¹, 1 bar, 200–900 °C.
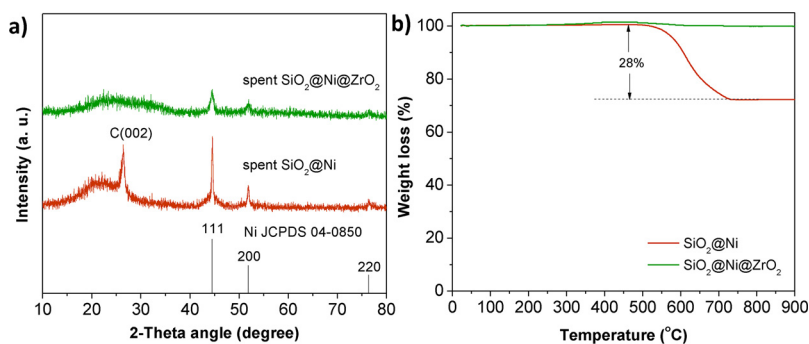
Fig. 5. (a) XRD patterns of spent $SiO_2@Ni$ and spent $SiO_2@Ni@ZrO_2$ catalysts after dry reforming reaction. (b) TGA of spent $SiO_2@Ni$ and spent $SiO_2@Ni@ZrO_2$ catalysts after dry reforming reaction. Reaction condition: 20 mL/min of CH_4, 20 mL/min of CO_2, 20 mL/min of N_2, total flow rate = 60 mL/min, 50 mg of catalyst, WHSV = 72,000 mL g^{-1} h^{-1}, 1 bar, 700 °C.
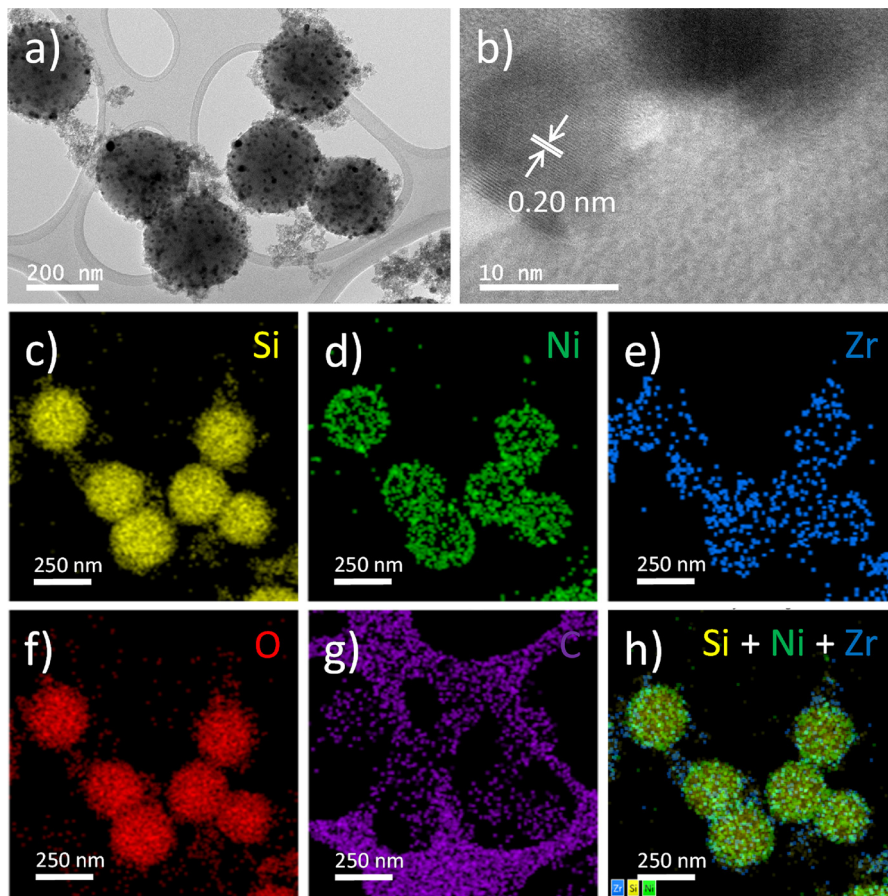

Fig. 6. (a, b) TEM images and (c–h) EDX mapping of spent $SiO_2@Ni@ZrO_2$ catalyst after dry reforming reaction. Reaction condition: 20 mL/min of CH_4, 20 mL/min of CO_2, 20 mL/min of N_2, total flow rate = 60 mL/min, 50 mg of catalyst, WHSV = 72,000 mL g^{-1} h^{-1}, 1 bar, 700 °C.

carbon deposition on spent catalysts. As shown in Fig. 6, the general morphology of $SiO_2@Ni@ZrO_2$ catalyst remains almost unchanged after dry reforming reaction, with Ni nanoparticles uniformly dispersed on the surface of SiO_2 spheres and covered with ZrO_2 shell. The size of Ni nanoparticles slightly becomes larger as 10 nm. There is no carbon formation observed from EDX mapping of spent $SiO_2@Ni@ZrO_2$ catalyst, which is consistent with XRD and TGA results. The carbon shown in Fig. 6g is from the carbon film of the copper grid, which is evidenced by comparing Fig. 6a and g. However, large amount of carbon nanotubes appeared around spent $SiO_2@Ni$ catalysts (Fig. 7). The lattice spacing of 0.34 nm is attributed to (002) plane of graphitic carbon (JCPDS 41-1487). From EDX mapping, the catalyst surface, particularly regions with large Ni particles, is covered with carbon deposited during dry reforming reaction. Furthermore, discrete carbon nanotubes are also found, which surround $SiO_2@Ni$ spheres. It is noted that the pressure in the reactor gradually increased during methane dry

reforming over $Ni@SiO_2$ catalyst at 700 °C for 20 h, and the reactor was clogged at the end of reaction test, which is consistent with TGA result of 28% carbon deposition. As the formed carbon nanotubes segregated from the catalysts, which partially explains the unchanged activity of $SiO_2@Ni$ catalyst (Fig. S2). This work aims to utilize the surplus CH_4 from shale gas and greenhouse gas CO_2 to produce syngas mixture. The ratio of CH_4 and CO_2 could be easily varied by changing the flowrate of each reactants. By using other sources of methane and carbon dioxide such as landfill gas with CH_4 to CO_2 ratio higher than 1 [63,64], coking could be more severe comparing to CH_4/CO_2 mixture with 1:1 ratio used in this work, due to decomposition of methane to carbon.

The stability of $SiO_2@Ni@ZrO_2$ catalyst during dry reforming reaction at 700 °C was investigated for 150 h. Shown in Fig. 8, the conversion of CH_4 at 5 h is 58.7%, which remains almost unchanged as 57.8% at 150 h. For CO_2, the initial conversion at 5 h is 58.0%, which slightly reduces to 50.8% at 50 h. After that, the conversion of CO_2

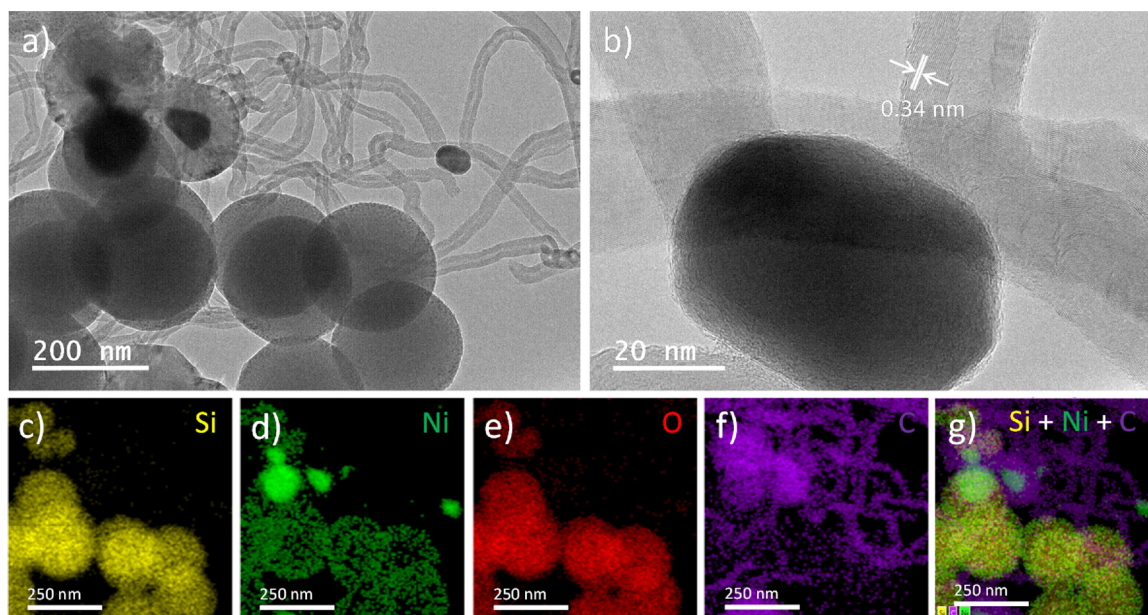**Fig. 7.** (a, b) TEM images and (c–h) EDX mapping of spent SiO$_2$@Ni catalyst after dry reforming reaction. Reaction condition: 20 mL/min of CH$_4$, 20 mL/min of CO$_2$, 20 mL/min of N$_2$, total flow rate = 60 mL/min, 50 mg of catalyst, WHSV = 72,000 mL g^{-1} h^{-1}, 1 bar, 700 °C.

remains nearly unchanged as 47.7% at reaction time of 150 h.

4.3. In situ X-ray absorption spectroscopy study of SiO$_2$@Ni@ZrO$_2$ catalyst

The evolution of catalyst structure under reduction and reaction conditions was examined by operando X-ray absorption near edge structure (XANES) and extended X-ray absorption fine structure studies of Ni K-edge (Fig. 9). The Ni K-edge XANES spectrum of fresh SiO$_2$@Ni@ZrO$_2$ catalyst is similar as that of NiO standard, with an intense white line appearing at 8350.6 eV. The Ni K-edge energy measured at the first inflection point is 8342.3 eV, consistent with that of NiO [65]. Furthermore, a characteristic pre-edge peak is observed at 8332.6 eV in Ni K-edge spectrum, which is attributed to quadrupole 1s→3d transition [66,67]. The k^3-weighted EXAFS spectrum is presented in Fig. 9c, with curve fitting results shown in Fig. S5 and Table S1. Two major peaks are observed at 2.03 Å and 3.07 Å, which can be assigned to first Ni−O coordination shell and second Ni−Ni coordination shell,

respectively [68,69]. Both of the XANES and EXAFS spectra confirms that the fresh catalyst consists of NiO phase, as the fresh catalyst was prepared via calcination at 500 °C in air. The intensity of the white line decreases with increasing reduction temperature, indicating the reduction process from NiO to Ni. At 700 °C, the intensity of white line decreases significantly and the pre-edge peak at 8332.6 eV disappears, suggesting that NiO is reduced to metallic Ni [70]. As shown in the Fourier transformed EXAFS spectra (Fig. 9c), the peak corresponding to Ni−O coordination disappears. A new peak is observed at 2.47 Å, which is due to first shell Ni−Ni coordination [11,55]. The coordination number (CN) of Ni−Ni is calculated to be 8.8 ± 0.8 based on the best-fit values.

After reduction, the reactor was cooled to 400 °C in N$_2$ flow, followed by switching the gas to 5%CH$_4$/5%CO$_2$/90%N$_2$. As shown in Fig. 9b, the Ni K-edge XANES spectrum for SiO$_2$@Ni@ZrO$_2$ catalyst under reaction condition is similar as that of reduced catalyst. The peak at 2.49 Å is attributed to first shell Ni−Ni coordination (Fig. 9d), with
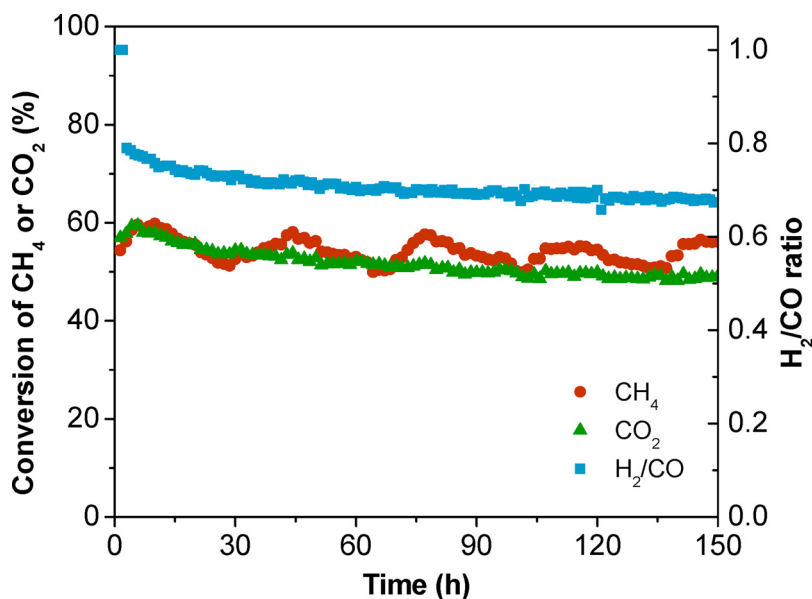

Fig. 8. Stability test of SiO$_2$@Ni@ZrO$_2$ catalysts for dry reforming of methane with carbon dioxide. Reaction condition: 10 mL/min of CH$_4$, 10 mL/min of CO$_2$, 10 mL/min of N$_2$, 75 mg of catalyst, WHSV = 24,000 mL g^{-1} h^{-1}, 1 bar, 700 °C. Red sphere stands for conversion of CH$_4$, green triangle stands for conversion of CO$_2$, and blue square stands for H$_2$/CO ratio. (For interpretation of the references to colour in this figure legend, the reader is referred to the web version of this article).
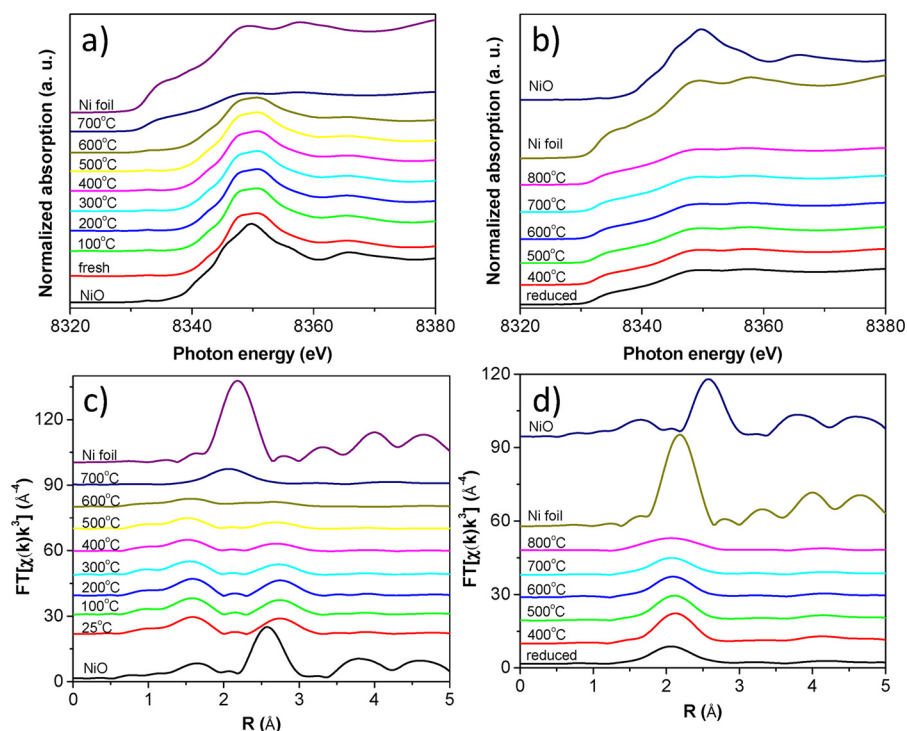
Fig. 9. Operando XANES/EXAFS study of SiO$_2$@Ni@ZrO$_2$ during (a, c) reduction and (b, d) methane dry reforming. Reduction condition: 1 mg of catalyst + 9 mg of SiO$_2$, 100 mL/min of 3.5%H$_2$/He, 25–700 °C at 5 °C/min. Reaction condition: 1 mg of catalyst + 9 mg of SiO$_2$, 100 mL/min of 5%CH$_4$/5%CO$_2$/N$_2$, 400–800 °C.
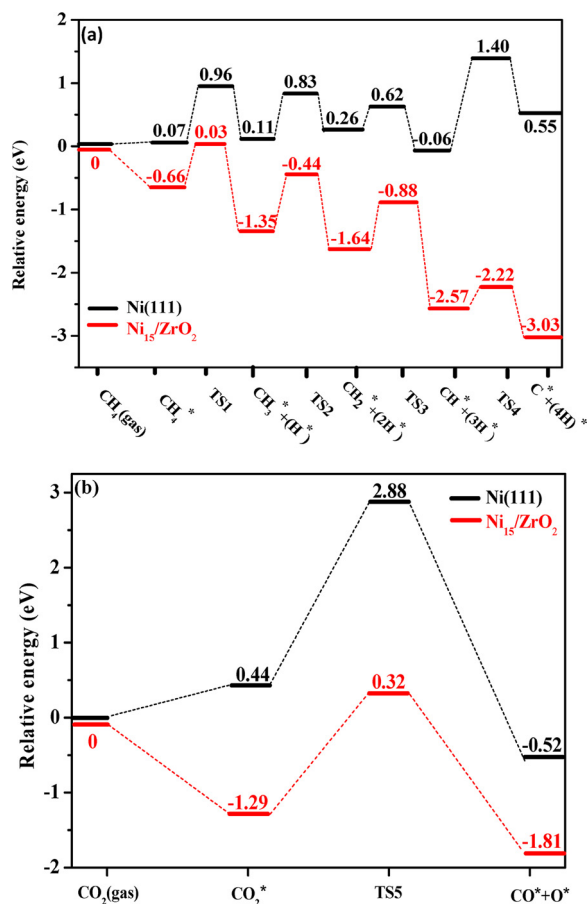

Fig. 10. The potential energy profiles for (a) CH$_4$ sequential dissociation and (b) CO$_2$ dissociation on Ni(111) and Ni$_{15}$/ZrO$_2$, respectively.

the CN of N−Ni as 9.4 ± 0.6. With increasing the reaction temperature to 800 °C, the XANES and EXAFS spectra remains almost unchanged. At 800 °C, the coordination number of Ni−Ni is 8.9 ± 1.0, suggesting that the metallic Ni remains also unchanged during dry reforming reaction at 400–800 °C (Fig. S6). It shows that the sandwiched structure of SiO$_2$@Ni@ZrO$_2$ cata₁yst is efficient for stabilization of Ni nanoparticles during reaction at high temperature.

## 4.4. Reaction pathway on SiO$_2$@Ni and SiO$_2$@Ni@ZrO$_2$ catalysts

Based on XRD, TEM and in-situ XAS studies, Ni(111) and Ni$_{15}$/ZrO$_2$ were selected as model catalysts to represent SiO$_2$@Ni and SiO$_2$@Ni@ZrO$_2$, respectively, for DFT calculations to understand the difference of reaction performance (i.e., activity and coke resistance) for methane dry reforming. Adsorption of reactants CH$_4$ and CO$_2$, the intermediates CH$_x$ (x = 0–3) and CO species in CO$_2$/CH$_4$ reforming reaction over Ni (111) and Ni$_{15}$/ZrO$_2$ were firstly investigated. The stable geometries of these species are schematically depicted in Fig. S8; the calculated adsorption energies, preferred adsorption sites and corresponding geometric parameters are listed in Table S2. The results show that all these species prefer to be adsorbed at the different sites of Ni$_{15}$ cluster rather than the ZrO$_2$ and the interfacial site between the Ni particles and the zirconia; in addition, when the species are initially adsorbed at the interfacial site between Ni particles and the zirconia, after geometry optimization, the species migration from the interfacial site to the Ni cluster occurs. Further, all reactions considered in this study showed that the transition state of the reaction also interact with the Ni$_{15}$ cluster. Thus, the Ni$_{15}$ cluster is the preferred adsorption site for all species and the active center for the reactions instead of the ZrO$_2$ and the interfacial site between Ni particles and the zirconia.

4.4.1. CH$_4$ sequential dissociation on Ni(111) and Ni$_{15}$/ZrO$_2$
Based on the stable adsorption configurations of the possible species, we then explored CH$_4$ dissociation in CH$_4$/CO$_2$ reforming reaction over Ni(111) and Ni$_{15}$/ZrO$_2$ catalyst, respectively. The calculated dissociation barriers (E_a) and reaction energies ($\triangle E$) are listed in Table S3.
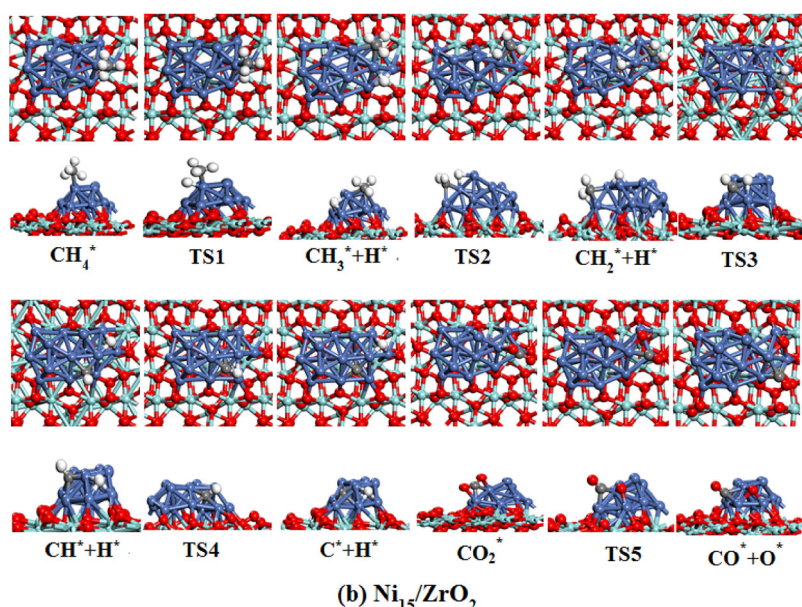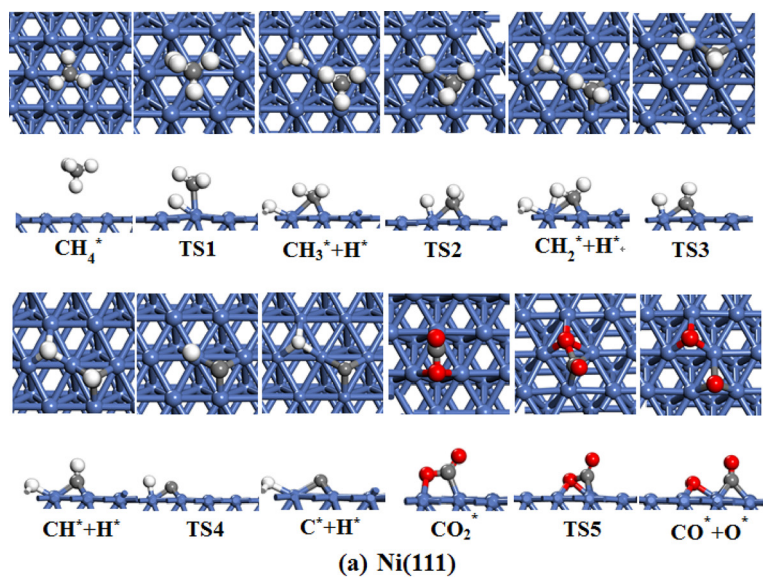
Fig. 11. The top and side view of the optimized geometries of the reactants, transition states (TS) and products for CH_4 sequential dissociation and CO_2 incomplete dissociation (a) Ni(111) and (b) Ni_{15}/ZrO_2, respectively (Ni, Zr, O, C and H atoms in blue, cyan, red, gray and white, respectively) (For interpretation of the references to colour in this figure legend, the reader is referred to the web version of this article).

The corresponding potential energies are shown in Fig. 10, and the structures of the reactant, transition state (TS) and product for the elementary step are presented in Fig. 11.

On Ni(111) surface, the adsorbed CH_4 dissociates into the co-adsorbed CH_3 and H species via a transition state (TS1), in which CH_3 locates at the top site and the dissociating H atom transfers to the hcp site. The C−Ni distance is shortened from 3.459 to 2.058 Å, while the C−H bond length is stretched from 1.097 to 1.605 Å. In the final state, CH_3 and H species are adsorbed at the fcc and hcp site, respectively. This process overcomes the dissociation barrier of 0.89 eV, and it is neutral in thermodynamics (0.04 eV). The adsorbed CH_3 further dissociates into CH_2 and H via TS2, in which the dissociating H atom shifts to the adjacent top site, CH_2 species adsorbs at the fcc site. The distance between C atoms and H atom is 1.792 Å. In the final state, CH_2 and H species are adsorbed at the fcc and hcp site, respectively. This reaction is slightly endothermic by 0.15 eV with the dissociation barrier of 0.72 eV. For the sequential dissociation of CH_2 into CH, followed by its

dissociation into C, in TSs, the breaking-up C−H bond lengths are 1.715 and 1.779 Å for CH_2 and CH dissociation, respectively. These two reactions have the reaction energies of −0.32 and 0.61 eV with the dissociation barriers of 0.36 and 1.46 eV, respectively.

On Ni_{15}/ZrO_2, the dissociation of adsorbed CH_4 at the top Ni_1 site into CH_3 and H proceeds through TS1, in which both CH_3 and H species bind to the Ni_1 atom with the shorter C−Ni bond length of 1.968 Å and the longer C−H bond length of 1.784 Å compared to those (2.251 and 1.111 Å) in adsorbed CH_4, respectively. In the final state, CH_3 and H species transfer to the two adjacent 3-fold hollow sites, respectively. This process is largely exothermic by 0.69 eV with the dissociation barrier of 0.69 eV. CH_3 can dissociates into CH_2 and H species via TS2, in which CH_2 and H species adsorb at the bridge site with the average C−Ni and H−Ni bond lengths of 1.900 and 1.714 Å, respectively; the distance between H atom to C atom is 1.650 Å. In the final state, CH_2 and H transfer to the two adjacent 3-fold hollow sites, respectively. The dissociation reaction is exothermic by 0.29 eV with the dissociation

barrier of 0.91 eV. For CH_2 dissociation, in TS3, the dissociating H atom binds to the Ni_1-Ni_{11} bridge site with the C−H distance of 1.548 Å, CH species locates at the 3-fold hollow site with the average C−Ni bond length of 1.853 Å. In the final state, H atom transfers to the 3-fold hollow site, and CH transfers to the 4-fold hollow site. The dissociation reaction is exothermic by 0.93 eV with the dissociation barrier of 0.76 eV. For CH species, it dissociates into C and H atom via TS4, in which the C–H bond length is elongated to 1.260 Å. The left C atom remains at the 4-fold hollow site, while the H atom shifts to the adjacent 3-fold hollow site. This step is exothermic by 0.46 eV and overcomes the dissociation barrier of 0.35 eV

4.4.2. CO_2 dissociation on $Ni(111)$ and Ni_{15}/ZrO_2

The dissociation barriers (E_a) and reaction energies ($\triangle E$) of CO_2 dissociation over Ni(111) and Ni_{15}/ZrO_2 catalyst are listed in Table S3. The corresponding potential energies are shown in Fig. 10; the optimized geometries of the reactants, transition states (TS) and products are illustrated in Fig. 11.

On Ni(111) surface, the adsorbed CO_2 can dissociate into CO and O species via TS5, where the CO species transfer to the adjacent bridge site from the original bridge site while the left O atom migrates to the fcc site with the dissociating C−O distance of 1.592 Å. The average C−Ni and O−Ni bond lengths are 1.978 and 1.974 Å, respectively. In the final state, CO adsorbs at the fcc site and O atom locates the fcc site with the average C−Ni and O−Ni bond length of 1.838 and 1.973 Å, respectively. This reaction has the high dissociation barrier of 2.44 eV, and it is exothermic by 0.96 eV.

On Ni_{15}/ZrO_2, the adsorbed CO_2 dissociates into the adsorbed CO and O species via TS5, in which CO species is adsorbed at the adjacent bridge site with the average C−Ni bond length of 1.867 Å, and the left O species is at the bridge site. Meanwhile, the C−O bond length is stretched from 1.254 to 1.855 Å in TS5. In the final state, CO and O species migrates to the adjacent 3-fold hollow site with the average C−Ni and O−Ni bond length of 1.952 and 1.861 Å, respectively. This step needs to overcome the dissociation barrier of 1.61 eV and it is exothermic by 0.52 eV.

4.4.3. The comparison of CH_4 and CO_2 dissociation between $Ni(111)$ and Ni_{15}/ZrO_2

In order to obtain the effect of the particle size on the catalytic activity, the activity of CH_4/CO_2 reforming reaction on Ni_{15}/ZrO_2 and Ni(111) structure were compared by the highest barrier for CH_4 sequential dissociation and CO_2 dissociation. As shown in Fig. 10, with respect to the gas phase CH_4, the highest dissociation barrier of CH_4 sequential dissociation into C is only 0.03 eV on Ni_{15}/ZrO_2, which is much lower by 1.37 eV than that (1.40 eV) on Ni(111) surface. The obvious decrease of dissociation barrier indicates that Ni/ZrO_2 catalyst has much higher catalytic activity toward CH_4 dissociation than Ni (111) surface, which well explains the experimental finding that drying reforming activity is improved by 5–7 times after coating with ZrO_2. On the other hand, for CO_2 dissociation into CO, the larger decrease of 2.56 eV for the highest barrier energy is also found from Ni_{15}/ZrO_2 to Ni(111), which also accords with the experimental result that CO_2 conversion is improved after coating with ZrO_2 and further indicates that the activity of Ni_{15}/ZrO_2 is obviously superior to the pure metal Ni for CO_2 dissociation. Therefore, Ni_{15}/ZrO_2 performs more excellent activity than bulk Ni surface for CH_4/CO_2 reforming reaction.

Furthermore, we compared the dissociation barriers and reaction energies of the elementary steps for CH_4 sequential dissociation and CO_2 dissociation on Ni_{15}/ZrO_2 and Ni(111) to probe into the mechanism of the excellent performance of Ni_{15}/ZrO_2. As shown in Table S3, it can be found that compared to Ni(111) surface, these elementary step releases much more energies for CH_4 sequential dissociation on Ni_{15}/ZrO_2. That is, there is the greater thermodynamic driving force on Ni_{15}/ZrO_2 than Ni(111), which are attributed to the obvious enhancement of the adsorption energies of CH_4 and $CH_x(x = 0–3)$ species on

Ni_{15}/ZrO_2 compared to those on Ni(111) surface. On the other hand, for CO_2 dissociation, compared to Ni(111) surface, Ni_{15}/ZrO_2 catalyst not only decrease the dissociation barrier (0.83 eV), but also increase the adsorption energy of CO_2. Namely, the greater thermodynamic and kinetic driving force on Ni_{15}/ZrO_2 make CO_2 dissociation more easier compared to Ni(111). In addition, the adsorption energy of CO_2 (−1.29 eV) is much higher than that of CH_4 (−0.66 eV) on Ni_{15}/ZrO_2, leading to catalyst surface enriched with CO_2; moreover, compared to Ni(111), CO_2 dissociation is more easier on Ni_{15}/ZrO_2, it is inferred that more O atoms from CO_2 dissociation can be obtained to interact with surface C from CH_4 dissociation to inhibit coke formation. On the other hand, the weak adsorption energy of CO_2 (0.44 eV) and CH_4 (0.07) is comparable on bulk Ni, leading to relatively lower CO_2/CH_4 ratio on bulk Ni surface comparing to that on Ni_{15}/ZrO_2 surface, CO_2 dissociation is difficult on bulk Ni surface compared to that on Ni_{15}/ZrO_2, surface C from CH_4 dissociation cannot be effectively eliminated, which may explain the coke formation observed.

5. Conclusions

In summary, sandwiched $SiO_2@Ni@ZrO_2$ catalyst has been developed using wet chemistry synthetic route. The porous ZrO_2 shell is essential for uniform dispersion and stabilization of 6 nm Ni nanoparticles in-between SiO_2 core and porous ZrO_2 shell. Without ZrO_2 coating, large Ni particles with size of 33 nm are formed on the surface of silica spheres. The ZrO_2 coated $SiO_2@Ni@ZrO_2$ catalyst exhibited excellent activity for methane dry reforming, with its activity 5–7 times higher than that of uncoated $SiO_2@Ni$ catalyst at 500–700 °C. In addition, the $SiO_2@Ni@ZrO_2$ catalyst is coke resistant, and very robust for extended reaction time. Operando XAS studies confirms $SiO_2@Ni@ZrO_2$ catalyst having metallic Ni phase under dry reforming reaction condition at $500-800$ °C. Density functional theory (DFT) calculations suggest that Ni_{15}/ZrO_2 not only reduce CO_2 dissociation barrier, but also effectively stabilize the reactants and the intermediates involving in CH_4/CO_2 reforming reaction, such as CH_4, CO_2, $CH_x(x = 0–3)$ and CO; as a result, Ni_{15}/ZrO_2 significantly reduces highest dissociation barrier of CH_4 and CO_2 and improve the catalytic activity for CH_4/CO_2 reforming reaction. Furthermore, the higher adsorption energy of CO_2 comparing to CH_4 and the lower dissociation barrier of CO_2 on $SiO_2@Ni@ZrO_2$ catalyst explains its coke resistance during methane dry reforming reaction.

Conflict of interest

The authors declare no competing financial interest.

Appendix A. Supplementary data

Supplementary material related to this article can be found, in the online version, at doi:https://doi.org/10.1016/j.apcatb.2019.05.021.

References

[1] D. Pakhare, J. Spivey, A review of dry (CO2) reforming of methane over noble metal

catalysts, Chem. Soc. Rev. 43 (2014) 7813–7837.

[2] L.C. Buelens, V.V. Galvita, H. Poelman, C. Detavernier, G.B. Marin, Super-dry re-forming of methane intensifies CO2 utilization via Le Chatelier's principle, Science 354 (2016) 449–452.

[3] T.D. Gould, A. Izar, A.W. Weimer, J.L. Falconer, J.W. Medlin, Stabilizing Ni cata-lysts by molecular layer deposition for harsh, dry reforming conditions, ACS Catal. 4 (2014) 2714–2717.

[4] G.A. Olah, A. Goeppert, M. Czaun, G.K.S. Prakash, Bi-reforming of methane from any source with steam and carbon dioxide exclusively to Metgas (CO–2H2) for methanol and hydrocarbon synthesis, J. Am. Chem. Soc. 135 (2013) 648–650.

[5] D. Baudouin, K.C. Szeto, P. Laurent, A. De Mallmann, B. Fenet, L. Veyre, U. Rodemerck, C. Coperet, C. Thieuleux, Nickel-silicide colloid prepared under mild conditions as a versatile Ni precursor for more efficient CO2 reforming of CH4 catalysts, J. Am. Chem. Soc. 134 (2012) 20624–20627.

[6] U. Oemar, Y. Kathiraser, L. Mo, X.K. Ho, S. Kawi, CO2 reforming of methane over highly active La-promoted Ni supported on SBA-15 catalysts: mechanism and ki-netic modelling, Catal. Sci. Technol. 6 (2016) 1173–1186.

[7] Z. Xie, B. Yan, S. Kattel, J.H. Lee, S. Yao, Q. Wu, N. Rui, E. Gomez, Z. Liu, W. Xu, L. Zhang, J.G. Chen, Dry reforming of methane over CeO2-supported Pt-Co catalysts with enhanced activity, Appl. Catal. B 236 (2018) 280–293.

[8] Z. Li, L. Mo, Y. Kathiraser, S. Kawi, Yolk–satellite–shell structured Ni–yolk@Ni@SiO2 nanocomposite: superb catalyst toward methane CO2 reforming reaction, ACS Catal. 4 (2014) 1526–1536.

[9] Z. Bao, Y. Lu, J. Han, Y. Li, F. Yu, Highly active and stable Ni-based bimodal pore catalyst for dry reforming of methane, Appl. Catal. A 491 (2015) 116–126.

[10] Q. Yan, Y. Lu, F. To, Y. Li, F. Yu, Synthesis of tungsten carbide nanoparticles in biochar matrix as a catalyst for dry reforming of methane to syngas, Catal. Sci. Technol. 5 (2015) 3270–3280.

[11] S. Zhang, S. Muratsugu, N. Ishiguro, M. Tada, Ceria-doped Ni/SBA-16 catalysts for dry reforming of methane, ACS Catal. 3 (2013) 1855–1864.

[12] S.A. Theofanidis, V.V. Galvita, M. Sabbe, H. Poelman, C. Detavernier, G.B. Marin, Controlling the stability of a Fe–Ni reforming catalyst: structural organization of the active components, Appl. Catal. B 209 (2017) 405–416.

[13] M.-S. Fan, A.Z. Abdullah, S. Bhatia, Utilization of greenhouse gases through carbon dioxide reforming of methane over Ni–Co/MgO–ZrO2: preparation, characteriza-tion and activity studies, Appl. Catal. B 100 (2010) 365–377.

[14] S.M. Kim, P.M. Abdala, T. Margossian, D. Hosseini, L. Foppa, A. Armutlulu, W. van Beek, A. Comas-Vives, C. Copéret, C. Müller, Cooperativity and dynamics increase the performance of NiFe dry reforming catalysts, J. Am. Chem. Soc. 139 (2017) 1937–1949.

[15] J. Rostrup-Nielsen, J.K. Nørskov, Step sites in syngas catalysis, Top. Catal. 40 (2006) 45–48.

[16] Z. Hou, J. Gao, J. Guo, D. Liang, H. Lou, X. Zheng, Deactivation of Ni catalysts during methane autothermal reforming with CO2 and O2 in a fluidized-bed reactor, J. Catal. 250 (2007) 331–341.

[17] D. Chen, R. Lødeng, A. Anundskås, O. Olsvik, A. Holmen, Deactivation during carbon dioxide reforming of methane over Ni catalyst: microkinetic analysis, Chem. Eng. Sci. 56 (2001) 1371–1379.

[18] K.O. Christensen, D. Chen, R. Lødeng, A. Holmen, Effect of supports and Ni crystal size on carbon formation and sintering during steam methane reforming, Appl. Catal. A 314 (2006) 9–22.

[19] B.J. O'Neill, D.H.K. Jackson, J. Lee, C. Canlas, P.C. Stair, C.L. Marshall, J.W. Elam, T.F. Kuech, J.A. Dumesic, G.W. Huber, Catalyst design with atomic layer deposi-tion, ACS Catal. 5 (2015) 1804–1825.

[20] Z. Shang, S. Li, L. Li, G. Liu, X. Liang, Highly active and stable alumina supported nickel nanoparticle catalysts for dry reforming of methane, Appl. Catal. B 201 (2017) 302–309.

[21] E. Baktash, P. Littlewood, R. Schomäcker, A. Thomas, P.C. Stair, Alumina coated nickel nanoparticles as a highly active catalyst for dry reforming of methane, Appl. Catal. B 179 (2015) 122–127.

[22] M.-G. Jeong, S.Y. Kim, D.H. Kim, S.W. Han, I.H. Kim, M. Lee, Y.K. Hwang, Y.D. Kim, High-performing and durable MgO/Ni catalysts via atomic layer deposition for CO2 reforming of methane (CRM), Appl. Catal. A 515 (2016) 45–50.

[23] J. Dou, Z. Bao, F. Yu, Mesoporous Ni(OH)2/CeNixOy composites derived Ni/CeNixOy catalysts for dry reforming of methane, ChemCatChem 10 (2018) 250–258.

[24] K. Song, M. Lu, S. Xu, C. Chen, Y. Zhan, D. Li, C. Au, L. Jiang, K. Tomishige, Effect of alloy composition on catalytic performance and coke-resistance property of Ni-Cu/Mg(Al)O catalysts for dry reforming of methane, Appl. Catal. B 239 (2018) 324–333.

[25] Y. Cao, P. Maitarad, M. Gao, T. Taketsugu, H. Li, T. Yan, L. Shi, D. Zhang, Defect-induced efficient dry reforming of methane over two-dimensional Ni/h-boron ni-tride nanosheet catalysts, Appl. Catal. B 238 (2018) 51–60.

[26] E. le Saché, L. Pastor-Pérez, D. Watson, A. Sepúlveda-Escribano, T.R. Reina, Ni stabilised on inorganic complex structures: superior catalysts for chemical CO2 recycling via dry reforming of methane, Appl. Catal. B 236 (2018) 458–465.

[27] C. Lin, J.B. Jang, L. Zhang, E.A. Stach, R.J. Gorte, Improved coking resistance of "Intelligent" Ni catalysts prepared by atomic layer deposition, ACS Catal. 8 (2018) 7679–7687.

[28] J. Zhang, F. Li, Coke-resistant Ni@SiO2 catalyst for dry reforming of methane, Appl. Catal. B 176–177 (2015) 513–521.

[29] Z. Li, Y. Kathiraser, J. Ashok, U. Oemar, S. Kawi, Simultaneous tuning porosity and basicity of nickel@nickel-magnesium phyllosilicate core-shell catalysts for CO2 reforming of CH4, Langmuir 30 (2014) 14694–14705.

[30] X. Zhao, H. Li, J. Zhang, L. Shi, D. Zhang, Design and synthesis of NiCe@m-SiO2 yolk-shell framework catalysts with improved coke- and sintering-resistance in dry

reforming of methane, Int. J. Hydrogen Energy 41 (2016) 2447–2456.

[31] Z. Li, Z. Wang, B. Jiang, S. Kawi, Sintering resistant Ni nanoparticles exclusively confined within SiO2 nanotubes for CH4 dry reforming, Catal. Sci. Technol. 8 (2018) 3363–3371.

[32] J.W. Han, J.S. Park, M.S. Choi, H. Lee, Uncoupling the size and support effects of Ni catalysts for dry reforming of methane, Appl. Catal. B 203 (2017) 625–632.

[33] J.M. Kim, S. Jun, R. Ryoo, Improvement of hydrothermal stability of mesoporous silica using salts: reinvestigation for time-dependent effects, J. Phys. Chem. B 103 (1999) 6200–6205.

[34] Y. Han, F.-S. Xiao, S. Wu, Y. Sun, X. Meng, D. Li, S. Lin, F. Deng, X. Ai, A novel method for incorporation of heteroatoms into the framework of ordered meso-porous silica materials synthesized in strong acidic media, J. Phys. Chem. B 105 (2001) 7963–7966.

[35] B. Ravel, M. Newville, ATHENA, ARTEMIS, HEPHAESTUS: data analysis for X-ray absorption spectroscopy using IFEFFIT, J. Synchrotron Rad. 12 (2005) 537–541.

[36] M. Newville, IFEFFIT: interactive XAFS analysis and FEFF fitting, J. Synchrotron Rad. 8 (2001) 322–324.

[37] G. Kresse, J. Furthmüller, Efficient iterative schemes for ab initio total-energy cal-culations using a plane-wave basis set, Phys. Rev. B 54 (1996) 11169–11186.

[38] G. Kresse, J. Furthmüller, Efficiency of ab-initio total energy calculations for metals and semiconductors using a plane-wave basis set, Comput. Mater. Sci. 6 (1996) 15–50.

[39] J.P. Perdew, K. Burke, M. Ernzerhof, Generalized gradient approximation made simple, Phys. Rev. Lett. 77 (1996) 3865–3868.

[40] J.A. White, D.M. Bird, Implementation of gradient-corrected exchange-correlation potentials in Car-Parrinello total-energy calculations, Phys. Rev. B 50 (1994) 4954–4957.

[41] G. Kresse, J. Hafner, First-principles study of the adsorption of atomic H on Ni (111), (100) and (110), Surf. Sci. 459 (2000) 287–302.

[42] G. Chiarotti, Physics of Solid Surfaces, Springer-Overflag, Berlin, 1995.

[43] C. Kittel, Introduction to Solid State Physics, Wiley, 1986.

[44] D. Sheppard, P. Xiao, W. Chemelewski, D.D. Johnson, G. Henkelman, A generalized solid-state nudged elastic band method, J. Chem. Phys. 136 (2012) 074103.

[45] D. Sheppard, R. Terrell, G. Henkelman, Optimization methods for finding minimum energy paths, J. Chem. Phys. 128 (2008) 134106.

[46] S. Grimme, Semiempirical GGA-type density functional constructed with a long-range dispersion correction, J. Comput. Chem. 27 (2006) 1787–1799.

[47] K.X. Yao, H.C. Zeng, Simultaneous chemical modification and structural transfor-mation of Stöber silica spheres for integration of nanocatalysts, Chem. Mater. 24 (2011) 140–148.

[48] S. Tang, X. Huang, X. Chen, N. Zheng, Hollow mesoporous zirconia nanocapsules for drug delivery, Adv. Funct. Mater. 20 (2010) 2442–2447.

[49] J. Dou, H.C. Zeng, Integrated networks of mesoporous silica nanowires and their bifunctional catalysis–sorption application for oxidative desulfurization, ACS Catal. 4 (2014) 566–576.

[50] J. Dou, H.C. Zeng, Targeted synthesis of silicomolybdic acid (Keggin acid) inside mesoporous silica hollow spheres for Friedel-Crafts alkylation, J. Am. Chem. Soc. 134 (2012) 16235–16246.

[51] K. Hadjiivanov, M. Mihaylov, D. Klissurski, P. Stefanov, N. Abadjieva, E. Vassileva, L. Mintchev, Characterization of Ni/SiO2 catalysts prepared by successive deposi-tion and reduction of Ni2+ ions, J. Catal. 185 (1999) 314–323.

[52] Y. Lou, M. Steib, Q. Zhang, K. Tiefenbacher, A. Horváth, A. Jentys, Y. Liu, J.A. Lercher, Design of stable Ni/ZrO2 catalysts for dry reforming of methane, J. Catal. 356 (2017) 147–156.

[53] M. Németh, D. Srankó, J. Károlyi, F. Somodi, Z. Schay, G. Sáfrán, I. Sajó, A. Horváth, Na-promoted Ni/ZrO2 dry reforming catalyst with high efficiency: details of Na2O–ZrO2–Ni interaction controlling activity and coke formation, Catal. Sci. Technol. 7 (2017) 5386–5401.

[54] Q.J. Chen, J. Zhang, Q.W. Jin, B.R. Pan, W.B. Kong, T.J. Zhao, Y.H. Sun, Effect of reflux digestion treatment on the catalytic performance of Ni–CaO–ZrO2 nano-composite catalysts for CO2 reforming of CH4, Catal. Today 215 (2013) 251–259.

[55] V.M. Gonzalez-Delacruz, R. Pereñiguez, F. Ternero, J.P. Holgado, A. Caballero, Modifying the size of nickel metallic particles by H2/CO treatment in Ni/ZrO2 methane dry reforming catalysts, ACS Catal. 1 (2011) 82–88.

[56] J.-M. Wei, B.-Q. Xu, J.-L. Li, Z.-X. Cheng, Q.-M. Zhu, Highly active and stable Ni/ZrO2 catalyst for syngas production by CO2 reforming of methane, Appl. Catal. A 196 (2000) L167–L172.

[57] J.A. Montoya, E. Romero-Pascual, C. Gimon, P. Del Angel, A. Monzón, Methane reforming with CO2 over Ni/ZrO2–CeO2 catalysts prepared by sol–gel, Catal. Today 63 (2000) 71–85.

[58] J.A. Lercher, J.H. Bitter, W. Hally, W. Niessen, K. Seshan, J.W. Hightower, W. Nicholas Delgass, E. Iglesia, A.T. Bell (Eds.), Stud. Surf. Sci. Catal. Elsevier, 1996, pp. 463–472.

[59] D. Liu, X.Y. Quek, W.N.E. Cheo, R. Lau, A. Borgna, Y. Yang, MCM-41 supported nickel-based bimetallic catalysts with superior stability during carbon dioxide re-forming of methane: effect of strong metal–support interaction, J. Catal. 266 (2009) 380–390.

[60] M.-G. Jeong, S.Y. Kim, D.H. Kim, S.W. Han, I.H. Kim, M. Lee, Y.K. Hwang, Y.D. Kim, High-performing and durable MgO/Ni catalysts via atomic layer deposition for CO2 reforming of methane (CRM), Appl. Catal. A 515 (2016) 45–50.

[61] Z. Bian, I.Y. Suryawinata, S. Kawi, Highly carbon resistant multicore-shell catalyst derived from Ni-Mg phyllosilicate nanotubes@silica for dry reforming of methane, Appl. Catal. B 195 (2016) 1–8.

[62] H. Ay, D. Üner, Dry reforming of methane over CeO2 supported Ni, Co and Ni–Co catalysts, Appl. Catal. B 179 (2015) 128–138.

[63] F. Barrai, T. Jackson, N. Whitmore, M.J. Castaldi, The role of carbon deposition on

precious metal catalyst activity during dry reforming of biogas, Catal. Today 129 (2007) 391–396.

[64] S.G. Gopaul, A. Dutta, Dry reforming of multiple biogas types for syngas production simulated using Aspen Plus: the use of partial oxidation and hydrogen combustion to achieve thermo-neutrality, Int. J. Hydrogen Energy 40 (2015) 6307–6318.

[65] M. Tada, N. Ishiguro, T. Uruga, H. Tanida, Y. Terada, S.-i. Nagamatsu, Y. Iwasawa, S.-i. Ohkoshi, μ-XAFS of a single particle of a practical NiOx/Ce2Zr2Oy catalyst, Phys. Chem. Chem. Phys. 13 (2011) 14910–14913.

[66] A. Anspoks, A. Kuzmin, Interpretation of the Ni K-edge EXAFS in nanocrystalline nickel oxide using molecular dynamics simulations, J. Non-Cryst. Solids 357 (2011) 2604–2610.

[67] A.N. Mansour, C.A. Melendres, M. Pankuch, R.A. Brizzolara, X-ray absorption fine structure spectra and the oxidation state of nickel in some of its oxycompounds, J. Electrochem. Soc. 141 (1994) L69–L71.

[68] A. Kuzmin, J. Purans, A. Rodionov, X-ray absorption spectroscopy study of the Ni K edge in magnetron-sputtered nickel oxide thin films, J. Phys. Condens. Matter 9 (1997) 6979.

[69] M.A. Peck, M.A. Langell, Comparison of nanoscaled and bulk NiO Structural and environmental characteristics by XRD, XAFS, and XPS, Chem. Mater. 24 (2012) 4483–4490.

[70] T. Margossian, K. Larmier, S.M. Kim, F. Krumeich, A. Fedorov, P. Chen, C.R. Muller, C. Coperet, Molecularly tailored nickel precursor and support yield a stable methane dry reforming catalyst with superior metal utilization, J. Am. Chem. Soc. 139 (2017) 6919–6927.